Flexible flapping systems: computational investigations into fluid-structure interactions

T. Fitzgerald **M. Valdez** **M. Vanella** **E. Balaras** **B. Balachandran**
balab@umd.edu

Department of Mechanical Engineering, University of Maryland
Maryland
USA

ABSTRACT

In the present work, the authors examine two computational approaches that can be used to study flexible flapping systems. For illustration, a fully coupled interaction of a fluid system with a flapping profile performing harmonic flapping kinematics is studied. In one approach, the fluid model is based on the Navier-Stokes equations for viscous incompressible flow, where all spatio-temporal scales are directly resolved by means of Direct Numerical Simulations (DNS). In the other approach, the fluid model is an inviscid, potential flow model, based on the unsteady vortex lattice method (UVLM). In the UVLM model, the focus is on vortex structures and the fluid dynamics is treated as a vortex kinematics problem, whereas with the DNS model, one is able to form a more detailed picture of the flapping physics. The UVLM based approach, although coarse from a modeling standpoint, is computationally inexpensive compared to the DNS based approach. This comparative study is motivated by the hypothesis that flapping related phenomena are primarily determined by vortex interactions and viscous effects play a secondary role, which could mean that a UVLM based approach could be suitable for design purposes and/or used as a predictive tool. In most of the cases studied, the UVLM based approach produces a good approximation. Apart from aerodynamic load comparisons, features of the system dynamics generated by using the two computational approaches are also compared. The authors also discuss limitations of both approaches.

NOMENCLATURE

$\mathbf{a}$	vector of accelerations of the states of the flexible structure
A_{ij}	influence coefficient of vortex j on control point i
A_x	amplitude of horizontal motion of the hover kinematics
A_θ	amplitude of rotational motion of the hover kinematics
$C_{(\cdot)}$	nondimensional force coefficient where (•) means L: Lift, D: Drag, F: Friction, PW: Power
DNS	Direct Numerical Simulation
$\hat{\mathbf{e}}_{(\cdot)}$	unit vector in the (•) direction
$f_{\tan}$	tangential stress on the surface of the body
G_j	circulation of the vortex panel j
$\mathrm{H}(r)$	Heaviside step function
I_A	moment of inertia of link A, with respect to the hinge point b
k	stiffness of the linear torsion spring at the hinge b
Δl	length of each panel bound on the body
L_c	chord length and length of the body
m_A	mass of link A of the body
$\mathbf{M}$	mass matrix
$\hat{\mathbf{n}}$	unit vector normal to surface
p	pressure
POD	proper orthogonal decomposition
$\mathbf{q}$	mode shape of the POD
$\mathrm{Q}_{(\cdot)}$	force along the (•) direction
r	distance in pseudo state-space
$\mathrm{R}_{(\cdot)}$	driving force in the (•) direction

Paper No. 3537. Manuscript received 2 February 2010, revised version received 13 March 2011, accepted 2 June 2011.

https://doi.org/10.1017/S000192400000628X Published online by Cambridge University Press

$\mathbf{R}$	position vector in the inertial frame
Re	Reynolds number
s	generic signal in time
$t, \Delta t$	time, finite time step
T	time of one hovering period
UVLM	unsteady, vortex lattice method
$\mathbf{V}$	fluid velocity
V_c	characteristic velocity
V_{Bi}	velocity of the body
$x, \Delta x, y, \Delta y$	spatial coordinates in the inertial frame and their respective incremental steps in a grid
α	relative angle between segments of body
γ_i	i-th time dependent modal coefficient of the POD expansion
$\delta_{(\cdot)}$	cutoff radius used in the UVLM for the 'free-lattice' and the 'bound-lattice'
$\eta_{(\cdot)}$	distance from point b to centroid of link A or B
θ, θ_0	angle of segment B with respect to the x-axis, the initial angle at $t = 0$
μ	fluid viscosity
ρ	density of the body
ρ_f	density of the fluid
σ	time constant for exponential damping on the amplitude of the prescribed kinematics
Ψ	velocity potential
ω	natural frequency of flexible structure
ω_f	forcing frequency of prescribed kinematics

1.0 INTRODUCTION

In recent years, flapping wing dynamics has attracted the attention of researchers from diverse fields. It is a common belief that insect and bird locomotions rely on the use of nonconventional aerodynamic mechanisms to produce the lift and thrust needed to propel them in air. Such unsteady mechanisms described first by Weis-Fogh[1], can be categorised as follows: (*i*) delayed stall, (*ii*) wake capture, (*iii*) rotational lift and (*iv*) added mass effect. In addition, it has also been suggested that elastic deformations may serve as another unsteady mechanism source to enhance the aerodynamic performance of insect wings. For a comprehensive recent survey of the field, the reader is referred to the review of Shyy, Aono, Chimakurthi, Trizila, Kang, Cesnick, and Liu[2].

Early attempts to understand phenomena associated with flapping wings relied on simplified, but insightful approaches and tools (e.g., Smith, Wilkins and Williams[3]). Many of these approaches and tools are based on theories and methods developed in the aeronautics field. These theories and methods include the blade-element theory and the actuator-disk theory (momentum theory), which are widely used for the study of propeller performance (e.g., Ellington[4], Weis–Fogh[1], Jensen[5], Spedding[6]); the thin aerofoil theory (e.g., DeLaurier[7]); and the lifting-line and lifting-surface methods (e.g., Betteridge and Archer[8]). These methods can only provide gross estimates of the generated forces and the flapping efficiency in terms of power consumption. Furthermore, in general, they are based on restrictive assumptions such as large aspect-ratio wings, small amplitude oscillations, small angles of attack and so on. In addition, none of these methods can be used to obtain information on the time evolution of the wakes; that is, the vortex structures generated due to flapping motions.

The rapid growth in computing capabilities over the past decade has enabled investigations based on viscous flow solvers. Wang[9] performed various simulations for two-dimensional immersed wings by using simple harmonic kinematics and wing section geometries. Wang, Birch and Dickinson[10] extended that study and compared two-dimensional computations with three-dimensional experiments. Recently, Miller and Peskin[11,12] showed the strong dependence of the fluid forces upon the Reynolds number and the kinematics in an idealised "clap and fling" motion observed in certain small insects. Three-dimensional viscous simulations have also been conducted. For example, Liu, Ellington, Kawachi, Van Den Berg and Wilmott[13], Sun and Tang[14] and Ramamurti and Sandenberg[15] have carried out simulations of the hovering of hawkmoth and drosophila wings.

Recenly, Żbikowski[16] and Ansari, Żbikowski and Knowles[17] developed analytic tools for studying the flapping phenomenon. These authors used a bound vorticity distribution over the surface of the wing and imposed the non-penetration condition on the surface to solve for the intensity of the distribution. This formulation also allows for the separation from the leading and trailing edges, through the imposition of the Kutta condition at both edges. Yu, Tong and Ma[18], employed a singularity distribution of sources and sinks on the body surface and discrete vortices in the wakes. Another less explored means of attacking the problem consists of surface singularity methods, such as panel methods. Three-dimensional simulations of insects have been carried out by Smith *et al*[3]. They used distributions of doublets and sources singularities on the wing and body surfaces and doublets to track the evolution of the wakes.

In the present study, the authors' aim is to compare the results obtained from two different computational approaches: (*i*) viscous simulations based on the Navier-Stokes equations for incompressible flow, where all spatio-temporal scales are directly resolved. Due to the latter feature, this approach is referred to as Direct Numerical Simulation (DNS). (*ii*) inviscid flow computation based on the unsteady vortex lattice method (UVLM). From a computational standpoint, the UVLM based approach is appealing as it costs just a fraction of a DNS based approach and this could be a strong reason for pursuing vortex-lattice like methods. However, the extent of applicability of the UVLM based approach is not clear. For instance, is a tool based on this approach, a valid one to use in the range of design Reynolds numbers for micro-air-vehicles (MAVs)? A related question is the following: What are the relative roles of viscous effects and vortex interactions in flapping related phenomena? These questions are addressed in this study.

2.0 COMPUTATIONAL AERODYNAMICS

2.1 Unsteady vortex lattice method (UVLM)

In high Reynolds number flows, a boundary-layer develops next to the body surface. The no-slip condition is satisfied on this surface and the action of viscosity is to cause the vorticity in this layer to diffuse normal to the surface. As the Reynolds number approaches infinity, due to progressive reduction of viscous diffusion, the boundary-layer approaches a layer of infinitesimal thickness and the body surface is covered with an infinitesimally thin vortex sheet. Furthermore, the absence of vorticity outside this vortex sheet allows the outer flow to be treated as an inviscid, potential flow. The above mentioned observations justify the use of the two-dimensional UVLM approach, in which the possibility of leading-edge separation is taken into account. The incompressible flow surrounding the flapping aerofoil is irrotational, except next to the solid boundaries of the wing and in the wakes.

The boundary-layers and the wakes are treated as sheets of vorticity, as illustrated in Fig. 1. A bound-vortex sheet represents the boundary-layer on the body surface. Free-vortex sheets represent the wakes. These two types of vortex sheets join where flow separation occurs. In this work, since the wing section is considered to be infinitesimally thin, only one vortex sheet is used to model the boundary layers on both surfaces. In addition, it is assumed that flow separation occurs at the leading and trailing edges of the aerofoil.

https://doi.org/10.1017/S000192400000628X Published online by Cambridge University Press

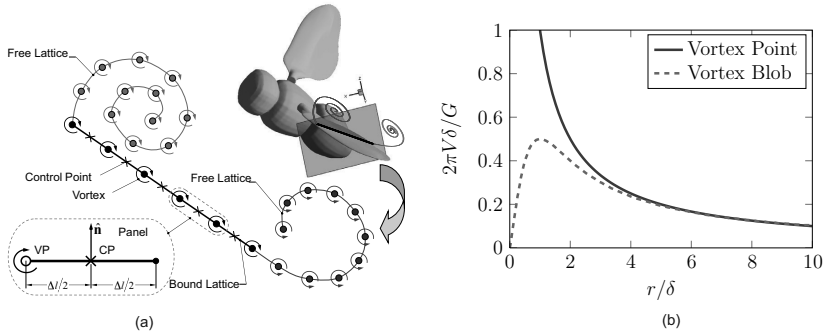


Figure 1. (a) Discretisation of bounded vortex sheets by panels and free vortex sheets by vortex points. (b) Radial variation of the velocity field for vortex point and vortex blob.

Vortex panel methods are based on the discretisation of the continuous vortex sheets into short, straight elements of concentrated vorticity. These elements must be short enough to ensure that the flow properties remain almost constant along their length. The vorticity of each element is concentrated at a single point vortex whose circulation is such that the non-penetration condition is satisfied at a point one-half of the element length away. As illustrated in Fig. 1, a point where the vortex is located is known as Vortex Point (VP) and a point where the non-penetration condition is imposed is referred to as Control Point (CP).

2.1.1 Formulation

The UVLM formulation is well established and the reader is referred to the text of Katz and Plotkin[19] and also the efforts of Preidikman, Valdez, Massa, Balachandran and Mook[20-23]. Outside the wakes and boundary-layers, the spatial-temporal evolution of the total velocity potential $\Psi(\mathbf{R},t)$ is governed by the Laplace equation

$$\nabla^2\Psi(\mathbf{R},t) = 0 \qquad \ldots(1)$$

and a set of boundary conditions (BCs). For a submerged body, the normal component of the fluid velocity relative to the surface must be zero on the surface of the body (no-penetration) and the disturbance created by the body motion should vanish far away from it. In addition, since the flow is irrotational and barotropic, subjected to conservative forces (due to gravity), Kelvin's circulation theorem applies; that is, the total circulation around a closed fluid path at every instant encloses the profile and its wakes remains constant in time.

The simultaneous imposition of the no-penetration condition at each control point together with Kelvin's circulation theorem leads to the following system of linear algebraic equations

$$\begin{aligned} &\sum_{j=1}^{N+1} A_j G_j(t) = -\left[\nabla\Psi_W - \mathbf{V}_B\right]_i \cdot \hat{\mathbf{n}}_i \qquad (i=1,2,\ldots,N) \\ &\sum_{j=1}^{N+1} G_j(t) = \sum_{j=1}^{N+1} G_j(t-\Delta t) \end{aligned} \qquad \ldots(2)$$

where V_{Bi}, $\hat{\mathbf{n}}_i$ and Ψ_W are the body-surface velocity, the unit normal vector and the velocity potential due to the vortices in the free–vortex sheets evaluated at the control point i, respectively and G_j is the circulation of the vortex panel j. The terms $\nabla\Psi_W$ and $\boldsymbol{V}_B$ are known from the previous time step and the kinematics, respectively. The solution of this system provides the circulations G_j around the vortices in each panel as well as that at the trailing edge G_{N+1}.

In order to satisfy the Kutta condition, at the end of each time step, the vortices located at the leading and trailing edges of the panel are shed into the flow field and they become part of the free vortex lattices. These vortices are convected with the local fluid particle velocity evaluated at the leading and trailing edges, respectively. This constitutes the flow separation model employed in this approach. Furthermore, the described convection process is employed to update the positions of the vortices that are already in the wake from previous time steps. In order to render the wake force–free, all of the vorticity must be transported with the fluid particles and vortex points in the wake must always be composed of the same fluid particles; that is, the strength of the free vortices remains constant in time.

It is important to note that the velocity field associated with a point vortex presents a singularity at the core. Therefore, at an evaluation point (vortex or control point), a point or disrete vortex approximation leads to amplification of numerical discretisation errors, eventually leading to a blowup. Choices for regularising this singularity include vortex-blob regularisation, vortex-patch regularisation, viscous regularisation and so on. In this work, the regularisation proposed by Krasny[24] is used to compute the influence of the vortices in the wakes upon one another and with the solid surfaces. In Figure 1, the radial variations of the vortex point velocity field and vortex blob velocity field are shown. Finally, in order to compute the aerodynamic loads, the jump in pressure across each element is obtained from the unsteady Bernoulli equation.

2.2 Direct Numerical Simulation (DNS)

The fluid dynamics is governed by the Navier-Stokes equation for incompressible flow; that is,

$$\frac{\partial\mathbf{V}}{\partial t} + \mathbf{V}\cdot\nabla\mathbf{V} = -\nabla p + \frac{1}{\mathrm{Re}}\nabla^2\mathbf{V} + \mathbf{f} \qquad \ldots(3)$$

$$\nabla\cdot\mathbf{V} = 0 \qquad \ldots(4)$$

where t is the time, p is the pressure and $\mathbf{f}$ is an external body force. The above equations have been made dimensionless by using the chord length of the undeformed structure, L_c, as the reference length scale and a characteristic translational velocity, V_c, as the reference velocity scale. The Reynolds number is defined as $\mathrm{Re} = \rho_f L_c V_c/\mu$, where ρ_f and μ are the fluid density and viscosity, respectively. The equations are discretised by using a second-order central finite-difference scheme on a structured Cartesian staggered mesh. The time integration is performed by using the fractional step method to

https://doi.org/10.1017/S000192400000628X Published online by Cambridge University Press

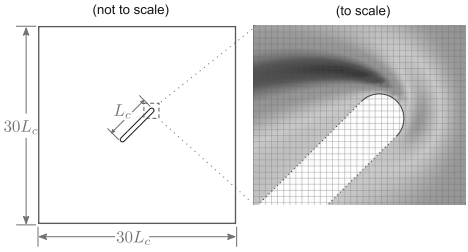


Figure 2. Schematic of the profile inside the DNS grid showing the overall size of the domain. The detailed view shows a close up near the leading edge of the body, where the red lines are grid lines, the black points are control points representing the body and the flow field is the magnitude of velocity for Re = 250, ω_f/ω = 1/2, at time t/T = 9·75.

ensure the incompressibility condition is met. The boundary conditions of the flapping profile, which is almost never aligned with the grid, are imposed by using an immersed boundary method. Details on the overall formulation can be found in Vanella and Balaras[25].

The computational grid was constructed to resolve the boundary-layers and other flow features on the moving profile. A schematic of the grid and an expanded view near the tip of the body is shown in Fig. 2. The centre point of the profile is located at the centre of a large box of dimensions $30L_c \times 30L_c$ to minimise the effects of the far-field boundary conditions. In the region that the profile moves through, the grid is uniform with the cell size $\Delta x = \Delta y = 3{\cdot}725 \times 10^{-3}\ L_c$. This cell size provides approximately 8 or 16 points inside the boundary for the low and high Reynolds number cases, respectively. The grid is then stretched to the boundaries. For the Re = 75 cases, the grid size is 1,229 × 551 and for the higher Reynolds number cases of Re = 250 and Re = 1,000, a higher resolution grid of 1,320 × 1,038 is used.

3.0 STRUCTURAL SYSTEM

The structural system is the same as the one used by Vanella, Fitzgerald, Preidikman, Balaras and Balachandran[26] and this system is shown in Fig. 3. It consists of two rigid links A and B, of equal length, joined at the centre b by a linear torsion spring. In the UVLM aerodynamic model employed here, bodies with infinitesimal thickness are used, whereas in the DNS work carried out by Vanella *et al*[26] bodies with finite thickness are used. In particular, the two rigid elements are covered by a set of aerodynamic surfaces that define the boundary between the aerofoil and the fluid. These surfaces deform as a consequence of the motions of the links. The aerodynamic surfaces consist of two rigid segments, R_{Sa} and R_{Sb} (see Fig. 3(b)) and these two segments dynamically deform according to the angle between the two rigid elements. Since the thickness constraint does not affect the UVLM model, these aerodynamic surfaces are not necessary. For the DNS work, a thickness of 10% L_c is used in most of the computations. To examine the effects of the thickness on the results, representative cases with a thickness of 3% L_c are also considered. For the purposes of the present work, the kinematics of link *B* are prescribed (both, translation and rotation) leaving the rotation of link *A* as the only degree of freedom of the system. The equation of motion describing the one degree-of-freedom structural system is;

$$I_A\ddot{\alpha} + k\alpha = -I_A\ddot{\theta} + m_A\eta_A \mathrm{Sin}(\theta+\alpha)\ddot{x} + Q_\alpha \qquad \ldots (5)$$

where $\alpha(t)$ is the deflection angle between links *A* and *B*. Here, m_A is the total mass of link *A*, η_A is the distance from the junction to the centre of mass of bar *A* as shown in Fig. 3(a) and I_A is the moment of inertia of link *A* with respect to the hinge point *b*. Q_α is the fluid moment associated with the generalised coordinate. Equation (5) has the form of a harmonic oscillator with a non-linear excitation due to the prescribed kinematics and the fluid forces (e.g., Nayfeh and Balachandran[27]), since *x*, *y* and θ are prescribed in time for hovering flapping. The nonlinearities arise from the sin (θ + α) term due to the kinematics and the fluid forcing.

4.0 FLUID-STRUCTURE INTERACTION

The communication between the fluid and the structure occurs through the generalised force Q_α in Equation (5). Both models are coupled and solved iteratively until convergence through a Hamming's predictor-corrector fourth-order scheme[28,29]. The overall algorithm is outlined in Fig. 4. The key features of this scheme are

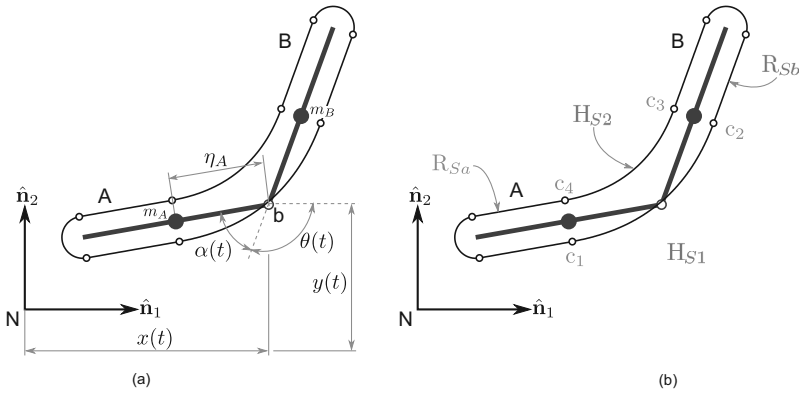


Figure 3. (a) The two-link model. The rigid links A and B (thick black line) are connected at hinge b by a torsion spring with stiffness *k*. The variables $x(t)$, $y(t)$, $\theta(t)$ and $\alpha(t)$ are the generalised coordinates used to describe the wing's motion. In the hovering simulations, $x(t)$, $y(t)$ and $\theta(t)$ are prescribed and $\alpha(t)$ is the only degree of freedom needed to define the system. (b) Decomposition of the wing's aerodynamic surfaces into rigid and deformable sections for the immersed-boundary scheme. R_{Sa} and R_{Sb} are connected at points c_1, c_2, c_3 and c_4 by Hermite interpolating polynomials H_{S1} and H_{S2}.

https://doi.org/10.1017/S000192400000628X Published online by Cambridge University Press

that full communication of the fluid and structure is considered and the procedure is independent of fluid model, structural model, or the number of bodies. The action of the fluid on the structure occurs through the generalised forces and the structure's action on the fluid is captured in the form of a kinematic boundary condition inside the fluid.

The process is started by advancing a single time step on the structural system. The states of the structural model define the positions and velocities of the surface of the body which are tracked at discrete points along the surface. The surface kinematics are then used as immersed boundary conditions on the fluid model. Next, the fluid is integrated one step forward in time and the fluid forces are then computed on the marker points defining the body. Holding time fixed, these new loads are applied to the structural equations of motion[5], leading to a corrected state of the system. The algorithm continues in the inner loop of Fig. 4 until the difference between successive iterations is less than a specified threshold.

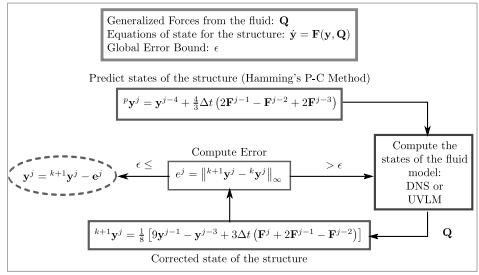


Figure 4. Process diagram outlining the fluid-structure coupling procedure to ensure two-way interactions.

5.0 COMPARATIVE STUDIES AND DISCUSSION

5.1 Prescribed kinematics and parameters

The kinematics consists of harmonic motions that involve translation and rotation of the top segment of the profile and this kinematics is representative of symmetric hovering of a cross-section of a flapping insect wing. The centre of rotation of the system of two links is located at the centre of the wing section (joint). The aerofoil rotation is in phase with the translation. The ratio of the translation amplitude to the chord length is . The equations that prescribe the kinematics are similar to others found in the literature for symmetric hovering[10] and given by;

$$x(t) = \left(1 - e^{-\frac{t}{\sigma}}\right)\frac{A_x}{2}\,\mathrm{Cos}\left(\omega_f t\right)$$
$$\theta(t) = \theta_0 + \left(1 - e^{-\frac{t}{\sigma}}\right)A_\theta\,\mathrm{Sin}\left(\omega_f t\right) \qquad \ldots (6)$$

where $x(t)$ is the global co-ordinate of the centre of the aerofoil, $\theta(t)$ is the orientation of link A with respect to the positive x axis (see Fig. 1) and ω_f is the flapping or forcing frequency defined as;

$$\omega_f = \frac{1}{A_x/2}. \qquad \ldots (7)$$

This ensures a maximum translation speed of one at the centre point of the structure and allows for direct non-dimensionalisation in terms of this characteristic speed. The amplitude of rotation A_θ is set to $\pi/4$ and the initial angle θ_0 is set to $-\pi/4$. The exponential growth term with time constant is used to give a non-impulsive start to the computations. The time constant τ is chosen such that 99·8% of the prescribed amplitude is reached after the duration of $5T$, where $T = 2\pi/\omega_f$ is the period of flapping. Similar values have been used in earlier work of the authors[26].

The system parameters are reduced to the following non-dimensional quantities: the Reynolds number, Re, for the DNS studies, the ratio of densities of the fluid to the structure, ρ/ρ_{fluid} and the ratio of the forcing frequency to the natural frequency of the structure, ω_f/ω. The density ratio is set to $\rho_s/\rho_f = 25$. This value is such the ratio of maximum translational inertia force over maximum drag force close to 2 in the Re =75 case, for the chosen geometry and kinematics. It was obtained through numerical experiments with a rigid two-dimensional profile[26]. Here, particular attention is paid to the frequency ratio, since this directly varies with the compliance of the structure. This ratio is defined as;

$$\frac{\omega_f}{\omega} = \frac{2/A_x}{\sqrt{k/I_A}}. \qquad \ldots (8)$$

It is through the selection of this ratio that the spring stiffness k is chosen, for fixed values of other parameters. The following values were chosen to cover a range from a very soft spring to an almost rigid spring: $\omega_f/\omega \in \{1/2, 1/3, 1/4, 1/6\}$. For the DNS studies, the Reynolds numbers used take the values in the set $\mathrm{Re} \in \{75, 250, 1000\}$. This parametric range has been chosen to cover flows extending from low Reynolds numbers, where viscous effects and dissipation are significant, to moderate Reynolds numbers.

In Fig. 5, for Re = 1,000 and $\omega_f/\omega = 1/3$, the shape and location of the hovering profile is shown over a single flapping cycle in equal time intervals, as obtained from a DNS study. The top of the figure shows the right-to-left motion of the stroke and the bottom part of the figure shows the return.

For all UVLM studies, the discretisation of the bound-vortex sheet consists of 100 panels uniformly distributed on the aerofoil section. The cutoff radius parameters are taken as;

$$\delta_{free\text{-}latice} = 2{\cdot}0\Delta l \quad and \quad \delta_{bound\text{-}latice} = 0{\cdot}75\Delta l \qquad \ldots (9)$$

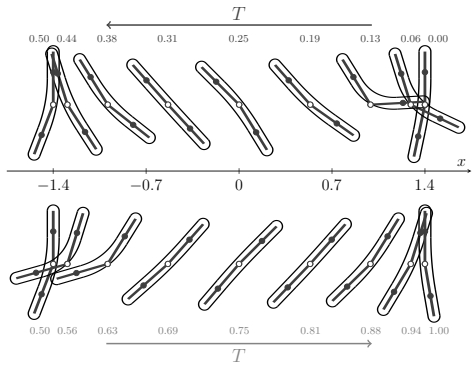


Figure 5. Characteristic motion of the profile with fluid-structure interaction for symmetric harmonic hovering. Depicted is the finite-thickness flexible configuration, at equally spaced intervals in time over one period of motion. These results have been obtained in a DNS study for Re = 1,000 and $\omega_f/\omega = 1/3$.

https://doi.org/10.1017/S000192400000628X Published online by Cambridge University Press

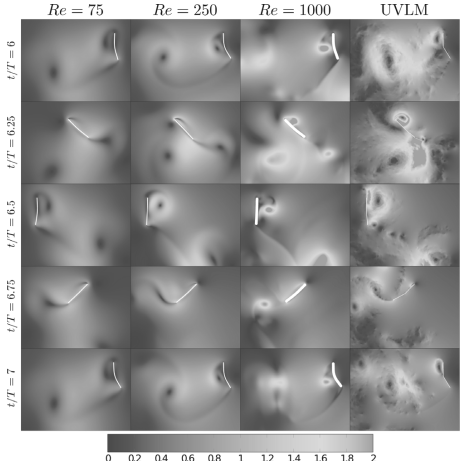


Figure 6. The magnitude of the velocity field at quarter intervals for period 6 determined from the DNS studies at Re = 75, 250, 1,000 and the UVLM study. The velocity field is normalised by the characteristic velocity of peak translation speed V_c. Similarities in both fluid and structure motions can be seen across Reynolds numbers and UVLM studies.

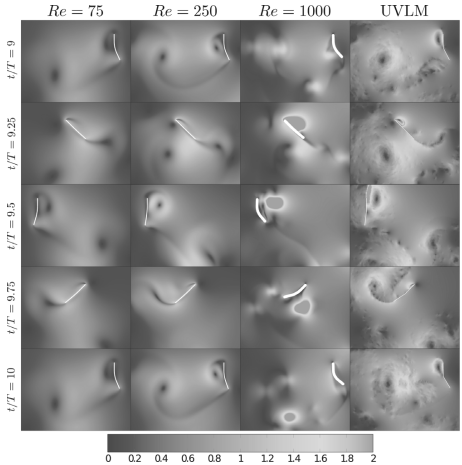


Figure 7. The magnitude of the velocity field at quarter intervals for period 9 for the DNS study at Re = 75, 250, 1,000 and the UVLM study. The velocity field is normalised by the characteristic velocity of peak translation speed V_c. It is noted that the results obtained at Re = 1,000 are distinctly different from the other results, while the UVLM results appear to be a blend of the Re = 250 and Re = 1,000 flow fields with a discernible presence of small scales.

where Δl is the length of a panel on the body. A convergence analysis of the UVLM runs demonstrated that over the first one and a half periods, the runs converged to a single solution. However, decreasing the step size past a certain point did not have any effect on the convergence of the solution past the first one and a half periods. It is believed by the authors that this fact is a consequence of the absence of dissipation in this inviscid formulation and the nonlinear wake to wake and wake to body interactions that take place in the phenomena under study. However, further analyses are needed to reach more precise conclusions on this matter. The number of time steps per period used in all UVLM studies is approximately 880. The DNS studies were carried out with constant time steps well below the Courant-Friedrichs-Lewy (CFL) condition, after some trials. The time steps per period are approximately 126×10^3, 44×10^3 and 9×10^3 for Re = 75, 250 and 1,000, respectively. From this point alone, the relative computational cost of the DNS study over the UVLM study is apparent. In addition, the UVLM approach can be parallelised more efficiently since each vortex can be independently tracked.

6.0 FLOW FIELDS

In Figs 6 and 7, a comparison between the flow fields obtained through the DNS studies for Re = 75, 250 and 1,000 and the UVLM studies is shown, for periods 6 and 9, respectively. For both figures, the ratio of the forcing frequency to the natural frequency of the system is chosen to be $\omega_f/\omega = 1/2$. The magnitude of the velocity field is shown, since the vorticity field is unavailable from the UVLM simulations. In these figures, the different vortex structures can be observed and compared as the viscous diffusion in the system is decreased. For Re = 75, the flow field snapshots throughout periods 6 and 9 are nearly identical, resulting in the periodicity of the flow field. This result is also supported by the $\alpha - \dot{\alpha}$ phase portrait of Fig. 13(a), in which a limit cycle can be seen for the same case analysed here. As a consequence, theaerodynamic loads generated by the profile are also periodic.

For Re = 250, the snapshots of the velocity appear to be very similar in periods 6 and 9. However, as shown later in the $\alpha - \dot{\alpha}$ phase portrait of Fig. 13(a), an exact periodic solution is not seen. There are small enough differences in the flow fields to cause small disturbances to what is nearly a periodic orbit. At Re = 1,000, as expected, the flow field is clearly no longer periodic since viscous diffusion becomes relatively small. However, the same kind of vortex structures can be identified as in the lower Reynolds number cases, such as the leading and trailing edge vortices. As expected, the intensity of these vortex structures increases, since they are proportional to the magnitude of the velocity. The non-periodicity of the flow field is a consequence of vortex interactions that were not dominant in the lower Reynolds numbers cases. In the latter cases, diffusion in the system spreads out the vorticity, so that vortex structures generated at the start of a flapping period are completely diffused by the end of it.

As the Reynolds number increases, the time scale of the diffusion process decreases as compared to that of the flapping period. Therefore, vortex structures created at the start of a flapping period still have some influence on the flow field after the end of that period. The nature of the interaction of the newly created vortex structures, with the old vortex structures present in the fluid is the cause of the breaking in the flow field periodicity. The velocity field obtained from the UVLM studies is able to capture most of the primary features found in the other flow fields. Although there are differences with the DNS results, it is emphasized that the method was able to predict qualitatively the vortex structures observed in the high fidelity DNS studies. The non-periodicity of the flow field observed at Re = 1,000 is also observed in the UVLM results and confirmed by the phase portrait

https://doi.org/10.1017/S000192400000628X Published online by Cambridge University Press

$\alpha - \dot{\alpha}$ of Fig. 13(a). An interesting observation was made when comparisons were made between the flow fields obtained at Re = 250 with those obtained through the UVLM studies. For period 9, in Fig. 7, the flow fields look qualitatively similar, judging by the location of the vortex cores, wakes and so on. The fact that in the UVLM simulations the vortex cores have low velocity is due to the regularisation method (cutoff) employed to avoid the numerical scheme to blow up. In Figure 1, the flow field obtained with the vortex blob regularisation technique is similar to that of a viscous vortex, with zero velocity at the core.

6.1 Aerodynamic loads

The lift and drag forces are defined here as being normal to and along the direction of the translational velocity of the aerofoil, respectively. Since the motion of the midpoint of the profile is confined to the horizontal plane, the lift and drag forces are coincident with the vertical and horizontal component of the aerodynamic force acting on the profile. The dimensionless drag and lift coefficients are defined as;

$$C_L(t) = \frac{Q_y(t)}{\frac{1}{2}\rho_f V_c^2 L_c} \qquad C_D = -\mathrm{sgn}\left(\dot{x}(t)\right)\frac{Q_x(t)}{\frac{1}{2}\rho_f V_c^2 L_c} \quad \ldots(10)$$

where Q_y and Q_x are the vertical and horizontal forces, respectively.

In Fig. 8, the temporal evolutions of the lift and drag coefficients are shown. The UVLM results are compared to the ones obtained from the DNS studies at Re = 1,000. The frequency ratio is 1/3 in both cases. It can be seen that during the starting interval (approximately one and a half period) the UVLM and DNS results are almost identical. As time evolves, however, the instantaneous values begin to diverge but they still follow some noticeable trends. The UVLM results successfully capture the dominant characteristics of the loads, with similar peaks and valleys in the lift coefficient corresponding to the mid-stroke and stroke reversals, respectively. The drag coefficient also appears to follow the same pattern of over-prediction seen in the lift coefficient obtained through UVLM studies. From a design perspective, knowing that the UVLM results matches the DNS results over a short period, suggests that it can be used for studying transient maneuvers, for example, those with a clap and fling mechanism[1]. However, for long time hovering, a statistical analysis is needed.

Considering the load time histories, the authors computed the phase averages with respect to the period T of one flapping cycle and the obtained results are shown in Fig. 9. The phase averages are based on data collected from periods 5 to 15 and hence, it is expected that the corresponding kinematics has reached is full amplitude and the motions are at a phase beyond the initial startup transients. At the stroke reversal (i.e., T = 1/2), there is a jump in the drag coefficient, which is not captured correctly by the UVLM study. A possible reason for the discrepancy is the fact that there is vortex interaction with the body surface at this point of the stroke; that is, wake capture and viscous effects play a more dominant role than at other locations in the cycle. For the high frequency ratios of $\omega_f/\omega = \omega \in (1/2, 1/3, 1/4)$; that is, the soft spring values, the curves generally line up more closely, particularly in the case of lift. The relative root-mean-square difference between the DNS and UVLM loads is summarised in Table 1. The differences appear to be smaller for compliant structures indicating that the UVLM model could be more useful for fully coupled fluid-structure interactions compared to prescribed motion cases.

To obtain a conservative estimate of the input power, the same approach as that used by the authors in earlier work[26] is employed. First, the driving force $R_x(t)$ in the x direction and the driving moment $R_\theta(t)$ in the θ direction were computed from the mass matrix from the equations of motion as;

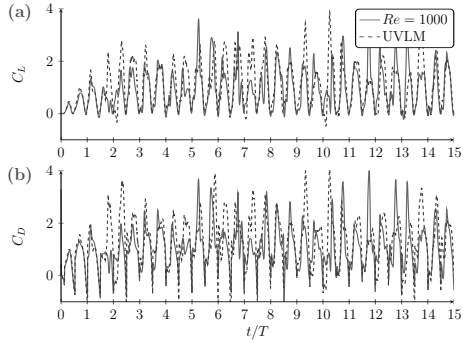


Figure 8. Instantaneous non-dimensional loads obtained from the DNS study at Re 1,000 (dashed lines) and the UVLM study (solid lines) with the frequency ratio set to $\omega_f/\omega = 1/3$. (a) Lift coefficient and (b) drag coefficient.

Table 1
Normalised RMS error values comparing the phase averaged loads from the UVLM study to those from the Re = 1,000 DNS study

RMS Error	ω_f/ω=1/2	ω_f/ω=1/3	ω_f/ω=1/4	ω_f/ω=1/6	Rigid
C_L	9·6%	13·4%	13·6%	25·6%	28·7%
C_D	9·9%	15·9%	10·0%	19·6%	24·7%

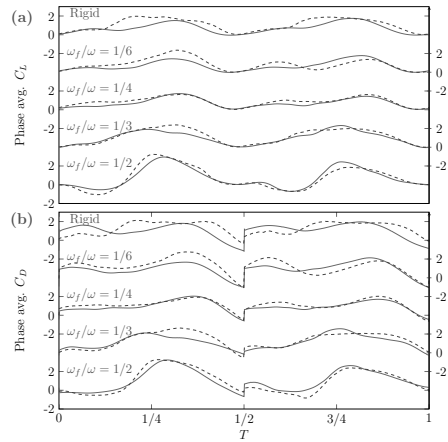


Figure 9. Phase averaged non-dimensional forces determined for various frequency ratios. Dashed lines are used to depict the UVLM study results and solid lines are used to depict the DNS study results at Re = 1,000. (a) Lift coefficient and (b) drag coefficient.

https://doi.org/10.1017/S000192400000628X Published online by Cambridge University Press

$$
\begin{aligned}
R_x(t) &= \hat{\mathbf{e}}_x^T \mathbf{M}\mathbf{a} - Q_x \\
&= (m_A + m_B)\ddot{x} + \left(-m_A\eta_a \mathrm{Sin}(\theta+\alpha) + m_B\eta_b \mathrm{Sin}\theta\right)\ddot{\theta} - m_A\eta_a \mathrm{Sin}(\theta+\alpha)\ddot{\alpha} \\
&\quad -\left(m_A\eta_a \mathrm{Cos}(\theta+\alpha)(\dot{\theta}+\dot{\alpha})^2 - m_B\eta_b\dot{\theta}^2\mathrm{Cos}\theta\right) - Q_x \\
R_\theta(t) &= \hat{\mathbf{e}}_\theta^T \mathbf{M}\mathbf{a} - Q_\theta \\
&= \left(-m_A\eta_A \mathrm{Sin}(\theta+\alpha) + m_B\eta_B \mathrm{Sin}\theta\right)\ddot{x} + (I_A + I_B)\ddot{\theta} + I_A\ddot{\alpha} - Q_\theta .
\end{aligned}
\qquad \ldots (11)
$$

Then, the input power is defined as;

$$
\begin{aligned}
P_{\mathrm{tr}}(t) &= \begin{cases} R_x\dot{x}, & \text{if} \quad R_x\dot{x} > 0 \\ 0, & \text{otherwise} \end{cases} \\
P_{\mathrm{rot}}(t) &= \begin{cases} R_\theta\dot{\theta}, & \text{if} \quad R_\theta\dot{\theta} > 0 \\ 0, & \text{otherwise} \end{cases}
\end{aligned}
\qquad \ldots (12)
$$

where $P_{tr}(t)$ is the translation power input and $P_{rot}(t)$ is the rotational power input. It is assumed that the power cannot be negative; that is, there is no power storage that absorbs output power. The non-dimensional power coefficient is then computed as;

$$
C_{\mathrm{PW}}(t) = \frac{P_{\mathrm{tr}}(t) + P_{\mathrm{rot}}(t)}{\frac{1}{2}\rho_f V_c^3 L_c}. \qquad \ldots (13)
$$

For both the DNS and UVLM studies, the overall time averages of the power coefficient are shown along with the aerodynamic loads in Fig. 10. All time averages have been computed over 10 cycles (from period 5 to 15). It is interesting to observe the peaks of the lift and drag coefficients at the frequency ratio , which were also observed in the authors' earlier work[26]. This trend is also qualitatively captured by the UVLM study. In Fig. 10(a), for all of the configurations, an increase in both the lift and drag over the rigid case is observed; however the UVLM study over-predicts both of these quantities by about 15%. When comparing the lift to drag ratio, shown in Fig. 10(b), the values match closely, since both quantities are equally over-predicted by the UVLM study. Finally, in Fig. 10(c), the overall efficiency, defined as the ratio of the average lift over the average power, is shown. There is good agreement between the results obtained from the DNS and UVLM studies. This indicates the usefulness of a computational approach such as that based on an UVLM approach for producing accurate estimates of the gross quantities important to a designer.

To determine to what extent the assumption of zero thickness of the profile is responsible for the above differences with the results of the DNS study, the authors conducted an additional

DNS study at Re = 1,000 with a profile thickness that is only 3% of the chord. The authors only considered a rigid case and computed the phase-averaged friction coefficient on the surface of the profile which is given by

$$
C_F = \frac{2}{\rho_f V_c^2} f_{\tan} \qquad \ldots (14)
$$

where C_F is the friction coefficient and f_{tan} is the tangential stress on the surface of the body. In Fig. 11, the authors show the mapping of these phase-averages to the aerodynamic surface at regular intervals during the hovering period. The black dots indicate locations where there is a change of sign in the phase-averaged C_F. It is noted that in the UVLM computations, the separation is always enforced at the leading/trailing edge. From the locations of these critical points, a separation is evident very close to the trailing edge throughout the entire stroke. The leading edge appears to have separation near the tip; however, this location moves during the cycle as the leading edge vortex grows and detaches from the surface. Although such complex dynamics cannot be reproduced by the UVLM study, they seem to dominate the production of the force coefficients over a relatively small part of the stroke cycle and as a result, the average force behavior is reproduced in a qualitative sense. The above results also indicate that perhaps no special separation models are needed in a UVLM study, at least, in the parametric range examined herein, beyond prescribing the locations of separations at the tips.

To better understand the features of the flow fields, the authors examined how the results of the DNS and UVLM studies compared

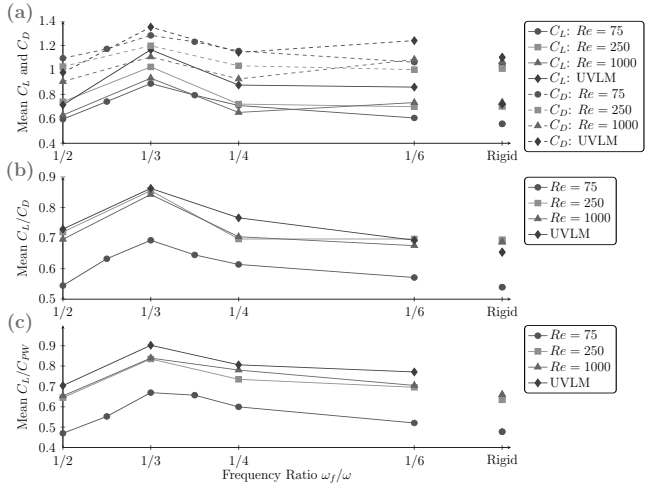


Figure 10. Comparisons of time averaged non-dimensional lift and drag coefficients obtained from the DNS study (Re = 75, 250, 1,000) and the UVLM study. (a) Mean lift and drag coefficients, (b) the ratio of mean lift to mean and (c) mean efficiency C_L/C_{PW}.

https://doi.org/10.1017/S000192400000628X Published online by Cambridge University Press

in terms of the coherent structures present in the fluid. For this examination, the authors used a method that produces the key spatial fluid patterns and allows for a hierarchical ranking of the fluid motions. This method is known as the proper orthogonal decomposition.

6.2 Proper orthogonal decomposition analysis

Proper orthogonal decomposition (POD) analysis is also referred to as the Karhunen-Loéve transform, principal component analysis, or singular systems analysis depending on the discipline. This analysis can be carried out in a continuous or discrete sense and used to study experimental[31] or computational[32] data. Here, the continuous formulation is applied to study computational data.

The overall aim of the POD analysis is to decompose data into a hierarchical set of spatial basis functions (mode shapes). Here, the velocity fields of the fluid are decomposed into spatial modes. To this end, the flow field is represented as;

$$\mathbf{V}(\mathbf{R},t) = \sum_{i=1}^{\infty} \gamma_i(t)\mathbf{q}(\mathbf{R}) \qquad \ldots (15)$$

This representation can be interpreted from a vibrations perspective as consisting of time-dependent coefficients, (γ_i), which are associated with modal coordinates, ($\mathbf{q}_i$). To construct the modes $\mathbf{q}(\mathbf{R})$, it is chosen to maximise the projection of the empirical data onto these modes in a L^2 sense. So, following earlier work[33], the problem statement is formulated in the scalar case as;

$$\max_{q \in L^2[0,1]} \frac{\left\langle \left| (V,q) \right|^2 \right\rangle}{\left| q^2 \right|}. \qquad \ldots (16)$$

where $(\cdot,\cdot)$ is the L^2 inner product on the domain of interest and $\langle\cdot\rangle$ is some averaging operation carried out on the ensemble of data. This all implies that q is chosen to maximise the energy contained in the original data. Following the method of snapshots[34], the results can be computed from the eigenvalues and eigenvectors of the autocorrelation of the velocity field snapshots.

Considering the first mode as the dominant mode in the predominant fluid motions, it is noted that across all configurations the same major structures are observed. The key fluid structures of interest are the downward jet associated with vertical lift and the

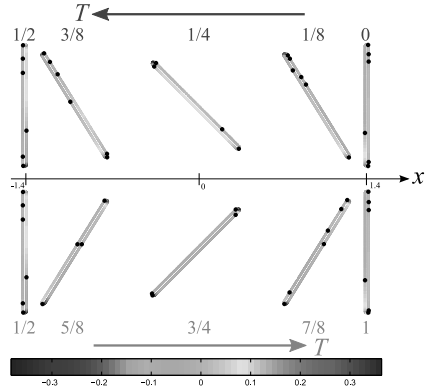


Figure 11. Coefficient of friction C_f on the surface of a rigid profile of 3% thickness; black dots indicate locations of sign changes.

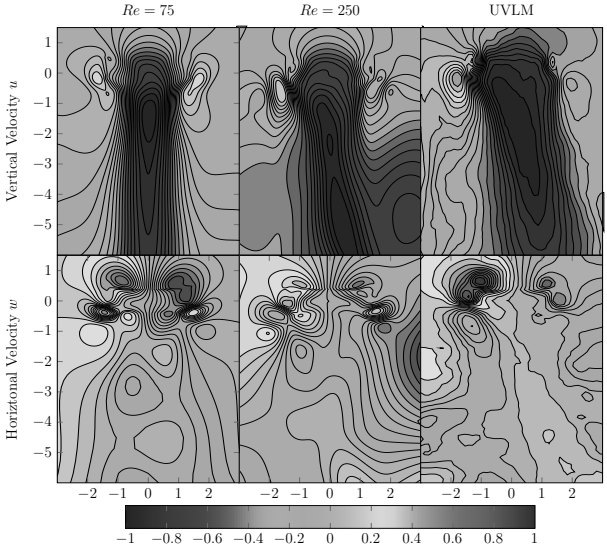


Figure 12. Mode 1 of the velocities obtained through proper orthogonal decomposition analysis for ω_f/ω = 1/3; results normalised so that $\max_{x,y \in \mathbf{R}} |\mathbf{q}| = 1$
Results from DNS studies are compared to those obtained through UVLM studies. The main structures (i.e., the downward jet, the end of stroke vortices and the leading edge vortices) are discernible in all cases.

https://doi.org/10.1017/S000192400000628X Published online by Cambridge University Press

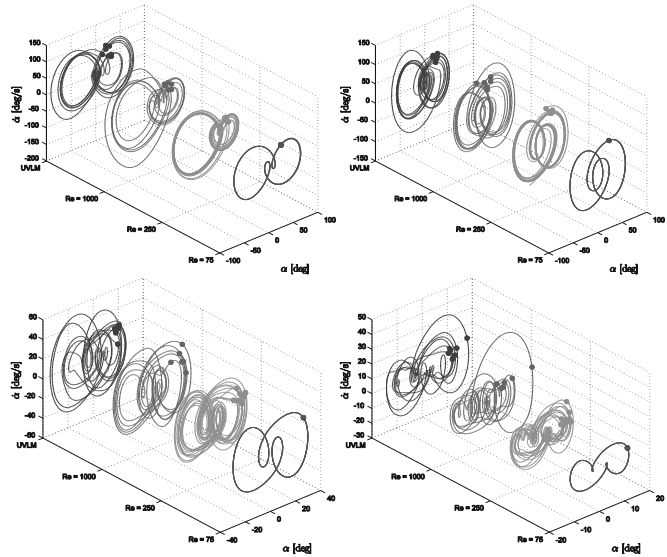


Figure 13. Phase portraits with Poincaré sections of $\alpha - \dot{\alpha}$ at several Reynolds numbers and frequency ratios: (a) ω_f/ω = 1/2, (b) ω_f/ω = 1/3, (c) ω_f/ω = 1/4, and (d) ω_f/ω = 1/6.

principal vortices associated with the flapping flight. These vortices include the vortex that is shed at the stroke reversal, known as the end of stroke vortex, as well as the influence of the leading and trailing edge vortices during the stroke. For $\omega_f/\omega = 1/3$, as can be discerned from Fig. 12, the predominant fluid structures seen in the low Reynolds cases are still preserved in the UVLM results.

In Fig. 12, the profile moves through $x = \pm 1{\cdot}4$ units and the centre connection of the two links is at $y = 0$. Also, these plots have been normalised so that the maximum absolute value of the velocity component is one. This provides a way to compare the intensities and spatial distributions of the fluid structures. The vertical velocity field shows a nice trend, with the low Reynolds number DNS cases showing more organisation and the high Reynolds number DNS cases containing wider structures. It is pointed out that in the high Reynolds number cases as well as in the UVLM case, there is a noticeable slight asymmetry of the downward jet. This is thought to be due to the lower dissipation allowing for more transients to be present in the flow.

On examining the dominant structures of the flow field, the UVLM studies appear to yield the major coherent structures that are observed in the DNS results even at low Reynolds numbers. Since the UVLM study is inviscid, one cannot compute and compare the vorticity fields of the POD modes in the usual fashion. However, by using the velocity component fields, one can shed light on the relative scales and the effects of dissipation[35].

7.0 FEATURES OF SYSTEM DYNAMICS

7.1 Phase portraits

To qualitatively examine the dynamics of the structure, the chordwise deformation α is considered. This measure gives insight into how the structure's response varies with respect to the two different fluid models and across various configurations. From the results depicted in Fig. 13, a natural trend can be observed in the $\alpha - \dot{\alpha}$ phase portraits shown from the softest spring case (i.e., ω_f/ω = 1/2) in frame (a) to the most firm spring case (i.e., ω_f/ω = 1/6) in frame (d). In each frame, there is a distinct trend observed with respect to Reynolds numbers. For the low Reynolds number cases, due to the viscous diffusion, which in turn acts over the structure as viscous drag, stable limit cycles are seen. However, with increase in the Reynolds number; that is, a decrease in viscous diffusion, there are changes in the character of the long time motions. The spacing amongst the intersection points on the Poincaré section, constructed by using a clock with the period T, is slightly wider and these intersections are more spread out. For the Re = 1,000 case, slightly higher velocities are seen and the points on the Poincaré section are widely spread out. It is interesting to note that in the inviscid UVLM study, the spacing of points on the Poincaré sections do not appear any wider than those seen for the DNS study conducted with Re = 1,000. This indicates that there may be some similarity or invariant characteristics imposed by the structural model and the prescribed kinematics.

On examining frame to frame in Fig. 13, although the structures are similar in shape, it is noted that the scales of each frame are different. As expected the higher frequency ratio yields the largest displacements and largest velocities. Furthermore, it is noted that the results obtained for the stiffest configuration $\omega_f/\omega = 1/6$ appear to be less organised at moderate to high Reynolds numbers. The authors have made comparisons in terms of system invariant characteristics such as the dimension of a motion in a recent study[36].

8.0 CONCLUSION

A comparison between two distinct computational approaches that can be used to study flapping wing systems has been presented in this article. One of these approaches is computationally expensive

https://doi.org/10.1017/S000192400000628X Published online by Cambridge University Press

while the other is coarse but computationally inexpensive. The use of these two computational approaches can be complementary in a design setting providing a multi-fidelity approach, since, the approximations obtained through the UVLM study are generally within 10-20% of the results obtained through high fidelity DNS studies. The gross aerodynamic quantities such as the mean lift and drag are over predicted by the UVLM study, but their ratio and the overall mean efficiency ratio predicted by the UVLM study agree well with those obtained in the DNS study. The POD studies showed that the UVLM approach captures most flow features observed in the DNS studies, among which, the most important is the vertical fluid jet represented by the first POD mode. This vertical jet is a clear evidence of the generation of lift by means of a flapping motion. In addition, flow field visualisations show that the UVLM study can be used for understanding the development and evolution of the different vortex structures. There are clear trends in the generated flow field as the Reynolds number of the flow is decreased since it loses its periodic character as the diffusion in the system decreases. This fact was also supported by the phase portraits constructed for the structural dynamics. In addition, it is observed from the phase portraits that as the diffusion in the system decreases, the amplitude of the relative motion between the passive and active parts of the structure increases. This result is expected since the diffusion in the fluid ultimately acts as a dissipative element, which takes energy out of the system.

The implication of the current study is that the UVLM study can be used as an inexpensive tool to qualitatively understand the physics of the flow related to flapping phenomena. This work can serve as foundation for developing tool boxes for the design and analysis of flexible flapping systems. It is noted that the UVLM based approach is several times faster than the DNS based approach, which means that a designer can study many more configurations of possible interest with this approach.

ACKNOWLEDGEMENTS

The authors gratefully acknowledge the partial support received for this work through the Cooperative Agreement FA86501023012 between the U.S. Air Force Research Laboratory, WPAFB, Ohio and the University of Maryland, College Park, Maryland.

REFERENCES

1. WEIS-FOGH, T. Biology and physics of locust flight. II. Flight performance of the desert locust (Schistocerca gregaria), *Philosophical Transactions of the Royal Society B*, 1965, **239**, pp 459–510.
2. SHYY, W., AONO, H., CHIMAKURTHI, S.K., TRIZILA, P., KANG, C.-K., CESNICK, C.E.S. and LIU, H. Recent progress in flapping wing aerodynamics and aeroelasticity, *Progress in Aerospace Sciences*, 2010, **46**, pp 284-327.
3. SMITH, M., WILKIN, P. and WILLIAMS, M. The advantages of an unsteady panel method in modelling the aerodynamic forces on rigid flapping wings. *J Experimental Biology*, 1996, **199**, pp 1073-1083.
4. ELLINGTON, C.P. The aerodynamics of hovering insect flight. Part V: A vortex theory. *Philosophical Transactions of the Royal Society B*, 1984, **305**, pp 115-144.
5. JENSEN, M. Biology and physics of locust flight. III. The aerodynamics of locust flight. *Philosophical Transactions of the Royal Society B*, 1956, **239**, pp 511–552.
6. SPEDDING, G.R. *The Aerodynamics of Flight. In Advances in Comparative and Environmental Physiology, 11, Mechanics of Animal Locomotion,* R.M. ALEXANDER (Ed), Springer, London, 1992, pp 51-111.
7. DELAURIER, J.D. An aerodynamic model for flapping-wing flight, *Aeronaut J*, 1993, **97**, pp 125-130.
8. BETTERIDGE, D.S. and ARCHER, R.D. A study of the mechanics of flapping flight, *Aeronaut Q*, 1974, **25**, pp 129–142.
9. WANG, Z.J. Two dimensional mechanism for insect hovering, *Physical Review Letters*, 2000, **85**, pp 2216-2219.
10. WANG, Z.J., BIRCH, J.M. and DICKINSON, M.H. Unsteady forces and flows in low Reynolds number hovering flight: two-dimensional computations vs robotic wing experiments, *J Experimental Biology*, 2004, **207**, pp 449-460.
11. MILLER, L. and PESKIN, C. When vortices stick: an aerodynamic transition in tiny insect flight, *J Experimental Biology*, 2004, **207**, pp 3073-3088.
12. MILLER, L. and PESKIN, C. A computational fluid dynamics of 'clap and fling' in the smallest insects, *J Experimental Biology*, 2005, **208**, pp 195-212.
13. LIU, H., ELLINGTON, C.P., KAWACHI, K., VAN DEN BERG, C. and WILLMOTT, A.P. A computational fluid dynamic study of hawkmoth hovering, *J Experimental Biology*, 1998, **201**, pp 461-477.
14. SUN, M. and TANG, J. Unsteady aerodynamic force generation by a model fruit fly wing in flapping motion, *J Experimental Biology*, 2002, **205**, pp 55-70.
15. RAMAMURTI, R. and SANDBERG, W.C. A three-dimensional computational study of the aerodynamic mechanisms of insect flight, *J Experimental Biology*, 2002, **205**, pp 1507-1518.
16. ŻBIKOWSKI, R. On aerodynamic modelling of an insect-like flapping wing in hover for micro air vehicles, *Philosophical Transactions of the Royal Society A*, 2002, **360**, pp 273-290.
17. ANSARI, S., ŻBIKOWSKI, R. and KNOWLES, K. Aerodynamic modelling of insect-like flapping flight for micro air vehicles, *Progress in Aerospace Sciences*, 2006, **42**, pp 129-172.
18. YU, Y., TONG, B. and MA, H. An analytic approach to theoretical modeling of highly unsteady viscous flow excited by wing flapping in small insects, *Acta Mechanica Sinica*, 2003, **19**, pp 508-516.
19. KATZ, J. and PLOTKIN, A. *Low-Speed Aerodynamics*, (2nd Ed), Cambridge University Press, 2001.
20. PREIDIKMAN, S. Numerical Simulations of Interactions among Aerodynamics, Structural Dynamics and Control Systems. Ph.D. Dissertation, Department of Engineering Science and Mechanics, Virginia Tech, Virginia, USA, 1998.
21. VALDEZ, M.F., PREIDIKMAN, S., MASSA, J.C., BALACHANDRAN, B. and MOOK, D.T. Aerodynamics of 2D Unsteady Vorticity Dominated Flows. 10th Pan American Congress of Applied Mechanics, 2008, **12**, pp 280-283.
22. VALDEZ M.F., PREIDIKMAN S. and MASSA J. Aerodynamics of two-dimensional and unsteady flows dominated by vorticity, *Computational Mechanics*, 2006, **24**, pp 2333-2357. (in Spanish).
23. VALDEZ M.F., PREIDIKMAN S. and BALACHANDRAN B. Two-dimensional Flapping wing aerodynamics: unsteady mechanisms, vorticity dominated flows and flight mechanisms. In preparation.
24. KRANSY, R. Computation of vortex sheet roll-up in the Trefftz plane, *J Fluid Mechanics*, 1987, **184**, pp 123–155.
25. VANELLA, M. and BALARAS, E. A moving-least-squares reconstruction for embedded-boundary formulations, *J Comput Physics*, 2009, **228**, pp 6617-6628.
26. VANELLA, M., FITZGERALD, T., PREIDIKMAN, S., BALARAS, E. and BALACHANDRAN, B. Influence of flexibility on the aerodynamic performance of a hovering wing, *J Experimental Biology*, 2009, **212**, pp 95-105.
27. NAYFEH, A.H. and BALACHANDRAN, B. *Applied Nonlinear Dynamics: Analytical, Computational and Experimental Methods*, Wiley, 1995.
28. PREIDIKMAN, S. and MOOK, D.T. On the development of a passive-damping system for wind-excited oscillations of long-span bridges, *J Wind Engineering and Industrial Aerodynamics*, 1998, **77-78**, pp 443-456.
29. YANG, J., PREIDIKMAN, S. and BALARAS, E. A strongly-coupled, embedded-boundary method for fluid-structure Interactions of elastically mounted rigid bodies. *J Fluids and Structures*, 2008, **24**, (2), pp 167-182.
30. DAGUM, L. and MENON, R. OpenMP: an industry standard API for shared-memory programming, *IEEE Comptational Science and Engineering*, 1998, **5**, pp 46-55.
31. TING, S.-C. and YANG, J.-T. Extracting energetically dominant flow features in a complicated fish wake using singular-value decomposition, *Physics of Fluids*, 2009, **21**, 041901.
32. O'DONNELL, B.J. and HELENBROOK, B.T. Proper orthogonal decomposition and incompressible flow: An application to particle modeling, *Computers and Fluids*, 2007, **36**, pp 1174-1186.
33. HOLMES, P., LUMLEY, J.L. and BERKOOZ, G. *Turbulence, Coherent Structures, Dynamical Systems and Symmetry*. Cambridge University Press, UK, 1996.

https://doi.org/10.1017/S000192400000628X Published online by Cambridge University Press

34. SIROVICH, L. Turbulence and the dynamics of coherent structures. Part I: Coherent Structures, *Quarterly of Applied Mathematics*, 1987, **45**, pp 561-571.
35. FITZGERALD, T., VALDEZ, M. and BALACHANDRAN, B. Flexible hovering wing motions: Proper orthogonal decomposition analysis. In 48th AIAA Aerospace Sciences Meeting Including the New Horizons Forum and Aerospace Exposition, Paper no. 2010-1027, Orlando, Florida, USA, 4–7 January, 2010.
36. FITZGERALD, T., VALDEZ, M. and BALACHANDRAN, B. A comparison of computational models for fluid-structure interaction of flexible flapping wing systems. In 49th AIAA Aerospace Sciences Meeting, Orlando, Florida, USA, 4–7 January, 2011.

https://doi.org/10.1017/S000192400000628X Published online by Cambridge University Press